

Towards ductilization of high strength 7XXX aluminium alloys via microstructural modifications obtained by friction stir processing and heat treatments

Matthieu B. Lezaack^a, Florent Hannard^a, Lv Zhao^{a,b}, Andrey Orekhov^{a,c,d}, Jérôme Adrien^e, Arttu Miettinen^{f,g,h}, Hosni Idrissi^{a,c}, Aude Simar^a

Corresponding author: Matthieu B. Lezaack,

Place Sainte Barbe, 2 bte L5.02.02, 1348 Louvain-la-Neuve, Belgique

E-mail corresponding author: matthieu.lezaack@uclouvain.be

^a Institute of Mechanics, Materials and Civil Engineering, Université catholique de Louvain, B-1348 Louvain-la-Neuve, Belgium

^b Department of Mechanics, School of Aerospace Engineering, Huazhong University of Science and Technology, Wuhan, China

^c Electron Microscopy for Materials Science (EMAT) University of Antwerp 2020 Antwerp, Belgium

^d NANOLab Center of Excellence, University of Antwerp, Belgium

^e MATEIS Lab, INSA de Lyon 69621 Villeurbanne cedex France

^f Institute for Biomedical Engineering, University and ETH Zurich, 8092 Zurich, Switzerland

^g Swiss Light Source, Paul Scherrer Institute, 5234 Villigen, Switzerland

^h Present address: Department of Physics, University of Jyväskylä, 40014 Jyväskylä, Finland

Abstract

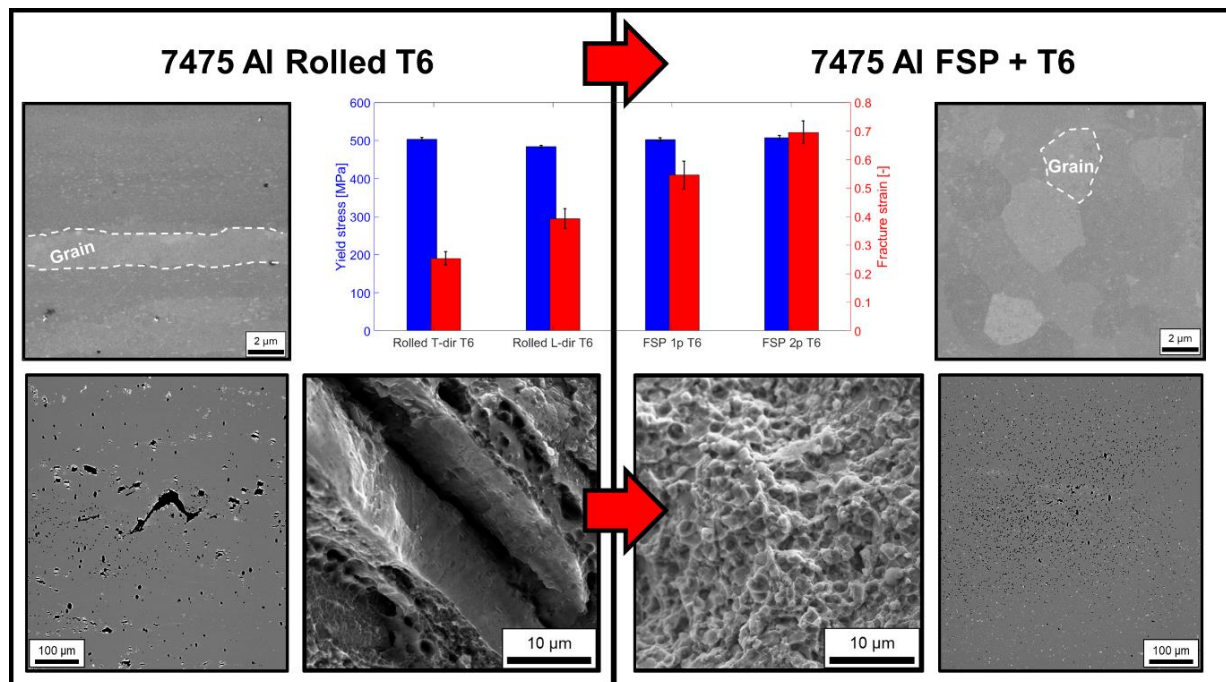
High strength 7XXX aluminium series reach exceptional strength, higher than all other industrial aluminium alloys. However, they suffer from a lack of ductility compared to softer series. This work presents a procedure to improve the ductility of 7475 Al alloy in high strength condition, reaching a true fracture strain of 70% at full 500 MPa T6 yield strength. Using friction stir processing (FSP) and post-FSP heat treatments, 100% of industrial rolled material T6 yield stress is maintained but a 180% increase in fracture strain is measured for the processed material. This ductility improvement is studied by in-situ synchrotron X-ray tomography and is explained by the reduction of intermetallic particles size and the homogenization of their spatial distribution. Furthermore, the microstructure after FSP shows equiaxed refined grains which favour crack deviation as opposed to large cracks parallel to the elongated coarse grains in rolled plate. These results are paving the way to better formability and crashworthiness of 7XXX alloys.

This document is the accepted manuscript version of the following article:

Lezaack, M. B., Hannard, F., Zhao, L., Orekhov, A., Adrien, J., Miettinen, A., ... Simar, A. (2021). Towards ductilization of high strength 7xxx aluminium alloys via microstructural modifications obtained by friction stir processing and heat treatments. *Materialia*, 20, 101248 (8 pp.).
<https://doi.org/10.1016/j.mtla.2021.101248>

This manuscript version is made available under the CC-BY-NC-ND 4.0 license <http://creativecommons.org/licenses/by-nc-nd/4.0/>

Graphical Abstract



Keywords

Aluminium alloys, Ductilization, Friction stir processing (FSP), Microstructure, Crack propagation

1. Introduction

7XXX aluminium alloys present the highest strength among aluminium-based industrial materials, playing a significant role in the aerospace industry [1]. $MgZn_2$ hardening precipitates allow the yield strength to reach over 500 MPa in T6 condition. In that state, precipitates are the semi-coherent η' phase and non-coherent η phase, as described by Aoba *et al.* [2] and Su *et al.* [3]. However, this precipitation does not occur homogeneously in the various aged tempers of 7XXX material [4][5]. Coarser η phases are formed during aging by preferential precipitation at grain boundaries (GB). GB precipitation leads to a depletion of alloying elements in the vicinity of the boundary, generating a softer precipitate-free zone (PFZ) (see supplementary **Figure S1a**) [5][6]. These PFZs have a first order effect on the mechanical properties of 7XXX alloys [4][5]. Recent work has demonstrated that the PFZ width may be reduced by adding Ag to the alloy composition [7], increasing the density of nucleation sites for hardening precipitates. Furthermore, the PFZ properties are sensitive to heat treatment process parameters. For example, fast quenching after solution heat treatment has been shown to reduce the PFZ width [4].

All 7XXX tempers are associated with a lower ductility in comparison with other series. The low ductility of 7XXX alloys is related to their damage mechanisms [5] (see supplementary **Figure S1b**). For most aluminium alloys, void nucleation originates from the fracture or interface decohesion of coarse impurities [5][8], such as iron-rich particles remaining after purification steps prior to alloy casting [9] (see **Figure S1b2**).

The damage sequence in 7XXX Al alloys can be described as follows. Ludtka *et al.* have shown that voids nucleate owing to the applied deformation [5]. The first microcracks formed by the coalescence of these voids then propagate in an intergranular manner (i.e. along grain boundaries) [5] (see **Figure S1b3**). Void nucleation and intergranular crack propagation are favoured by the softer PFZs and the coarser precipitates at GB (either η phase or E dispersoids) [5]. PFZs promote strain localization and act as a “pre-cut path” for crack propagation [5], like a zip decorated by coarse grain boundary precipitates. Finally, transgranular crack propagation (i.e. inside the grains) occurs linking these microcracks which triggers the final fracture of the specimen [5] (see **Figure S1b4**). The damage process results from an overlapping sequence of void initiation at GB impurities and coarse precipitates, intergranular decohesion and transgranular tearing. A more detailed description of this complex fracture process was given by Kamp *et al.* [10].

Furthermore, the effect of microstructure heterogeneities on damage accumulation in 7XXX series Al alloys has been studied by Wang *et al.* [11]. This analysis showed that in a partially recrystallized microstructure, the rolled elongated grains are cut by transgranular crack propagation while the equiaxed recrystallized grains undergo intergranular decohesion. The intergranular propagation on the recrystallized microstructure was explained by a higher high angle grain boundaries (HAGB) density. Indeed, HAGB are high energy boundaries, favouring grain boundary instability – and thus damage – compared to low angle grain boundaries or subgrain boundaries for the rolled elongated grains [11].

Friction stir processing (FSP) leads to significant grain refinement in the nugget zone (NZ) due to dynamic recrystallization [12][13]. FSP breaks iron-rich intermetallic particles (IM) into smaller fragments and homogenizes the particle distribution [14]. Thermomechanically affected zones (TMAZs), i.e. regions surrounding the NZ, present deformed grains due to material stirring. Conversely, the heat affected zones (HAZs) have neither seen plastic deformation nor grain size modifications but heat sensitive precipitates are there impacted by the process [15][16].

FSP is an interesting technique for the processing of composite coatings near the material surface as well as for local grain refinement [17]. It has been widely applied to aluminium, magnesium, copper, titanium alloys as well as steels [18].

To the best of the author's knowledge, no thermomechanical process solutions reported in literature succeeded in significantly increasing the ductility of 7XXX industrial plate material. In a previous study [19], we showed that the Vickers hardness and the yield strength of a friction stir processed Al 7475, performed with controlled heat cycle, can be restored to a T6 temper after solution heat treatment followed by aging without any sign of abnormal grain growth [19]. Heat cycle is tuned by modifying the backing plate thermal conductivity during FSP [19]. Taking advantage of the microstructural refinement obtained by FSP, the present investigation shows the potential of combining FSP and post-processing heat treatments to improve the ductility of Al 7XXX plates in high strength conditions.

2. Material and methods

Cold rolled 12 mm thick plates of Al 7475 in T7351 state (Base Material, BM) were studied. The chemical composition as measured by inductively coupled plasma optical emission spectroscopy (ICP) is as follows: 5.67% Zn, 2.20% Mg, 1.50% Cu, 0.08% Fe and 0.22% Cr.

FSP procedure is described in **Figure 1**. FSP was performed with a rotational speed of 300 RPM, an advancing speed of 100 mm/min and a 15.5 kN controlled vertical force. A tool made of a 10 mm long pin (see **Figure 1**) was tilted by 1° during processing. In order to avoid abnormal grain growth during post-FSP heat treatments, a stainless steel backing plate was used to reduce FSP temperature gradients through the plate thickness, as described in Lezaack *et al.* [19]. A second overlapping FSP pass was performed on selected plates after 30 minutes cooling.

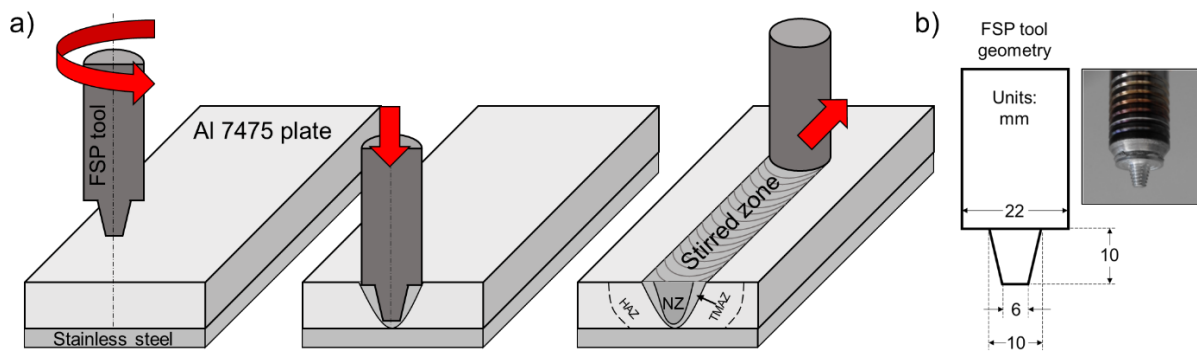


Figure 1: a) FSP schematic procedure, note the stainless steel backing plate placed below the 7475 plate: the stir zone is composed of a nugget zone (NZ) and a thermo-mechanically affected zone (TMAZ); themselves surrounded by a heat affected zone (HAZ). b) Tool geometry and picture, the pin is threaded with a tri flat shape.

All samples were then submitted to solution heat treatment at 470°C for 30 minutes followed by water quenching and subsequently artificially aged at 120°C for 24 hours in order to reach the peak-aged condition (T6 state). This T6 double step heat treatment is schematized on **Figure 2**.

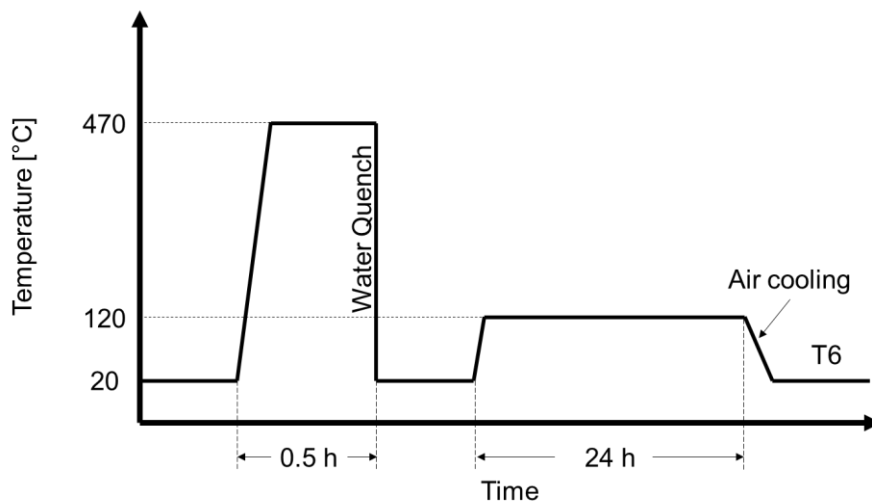


Figure 2: Schematic of the heat treatment applied on BM or after FSP leading to the T6 state.

Mirror-polished samples were observed by Ultra 55 FEG-SEM microscope. The intermetallic particles size distributions in the BM and FSPed microstructures were characterized based on SEM images. A threshold is set to extract iron-rich particles on a 10 mm² surface for each sample, the smallest detected particles are 1.55 µm in diameter.

Thermo Fisher Tecnai-Osiris transmission TEM microscope allowed observing the finest precipitates and the precipitate-free zones [20]. Samples were analysed by bright-field transmission electron microscopy (BF-TEM), high angle annular dark field scanning transmission electron microscopy (HAADF-STEM) and energy dispersive X-ray spectroscopy (EDXS). Electro polishing is used for samples preparation [2][20]. The average size of the hardening precipitates and PFZ width have been measured based on TEM images. 500 precipitates have been analysed.

Cylindrical 6 mm diameter tensile samples were extracted from the NZ along the FSP direction and along rolling direction (L-dir) and transverse direction (T-dir) for the BM. A 50 kN tensile machine loads the samples at 1 mm/min. Ductility was quantified by the true fracture strain as measured post-mortem on the broken specimens and defined as $\epsilon_f = \ln(A_0/A_f)$, with A_0 and A_f the initial and final samples sections.

In-situ X-ray tomography tensile testing was performed at the TOMCAT beamline (PSI, Switzerland) using a set-up described in [21]. This is a powerful tool for material science applications [22]. Visualization of the damage initiation and crack propagation was obtained on cylindrical notched-tensile samples of 1mm reduced diameter in T6 state. Isotropic voxel size is 320 nm × 320 nm × 320 nm.

3. Results

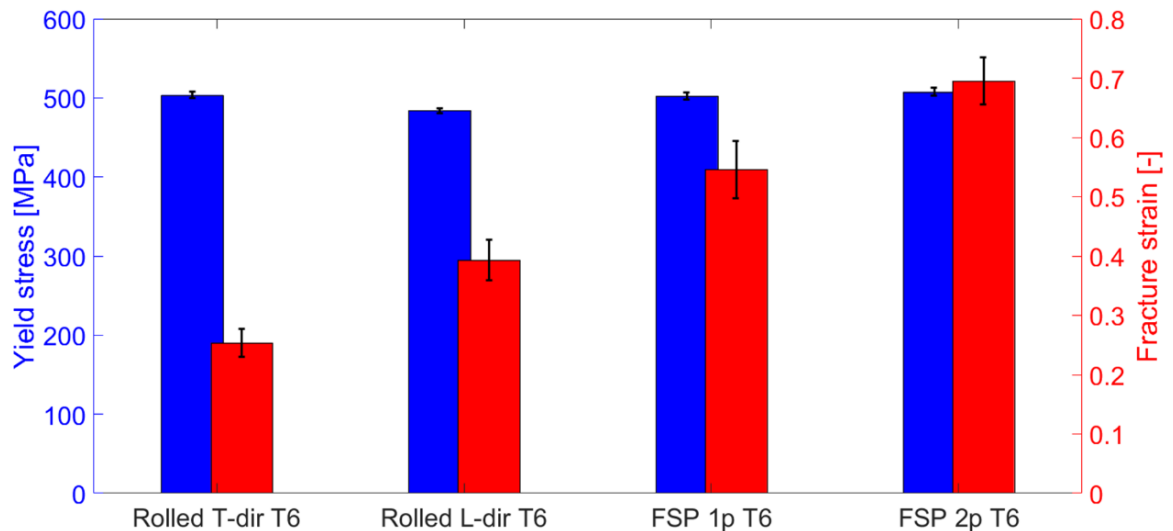


Figure 3: Yield strength and ductility of 7475 alloy and after 1 and 2 pass FSP-T6 heat treatment. Yield strength after FSP-T6 for both 1 and 2 pass is equivalent to the rolled material loaded in transverse direction (T-dir). Exceptional 180% increase in ductility is reached after 2 pass compared to rolled material T-dir.

Figure 3 shows the effect of FSP (1 and 2 pass) combined to T6 heat treatment on the tensile properties of 7475 alloy, in terms of yield strength and fracture strain (engineering tensile curves in supplementary **Figure S2a**). BM-T6 yield strength reaches 500 MPa in the transverse direction, associated with a 25% fracture strain. The highest fracture strain is observed after 2 pass FSP and T6 heat treatment, retrieving the yield strength level of the BM-T6 loaded along T-dir. FSPed 7475 materials present a fracture strain of 55% and 70% after 1 and 2 pass, respectively (true tensile curves in supplementary **Figure S2b**). Similar trends are observed for Al 7075 (supplementary **Figure S3**). A significant 180% ductility improvement is observed when comparing the rolled material and the 2 pass FSP samples.

The ultimate tensile strength of both FSP samples is close to that of the T6 rolled material loaded along the rolling direction (L-dir). The strain hardening is slightly affected by the modification of the microstructure after FSP (supplementary **Figure S2c** and **d** show a Voce law fitting [23] of the hardening curves). The dislocation storage and recovery rate parameters of this fit are only slightly affected by the FSP-T6 processing. The dislocation storage rate of the FSPed materials is actually similar to the dislocation storage rate of the BM-T6 loaded along L-dir, while the recovery rate of the FSPed materials stands in between the recovery rate of the rolled material loaded in L-dir and T-dir. The uniform elongation is also slightly different for the FSPed materials: 12% while rolled material uniform elongations are 13% and 14% for T-dir and L-dir respectively. In conclusion, the strain hardening rates of the FSP-T6 materials are not significantly different from that of the BM-T6 counterpart. Thus, the huge improvement in fracture strain after FSP-T6 cannot be explained by differences in strain hardening behavior.

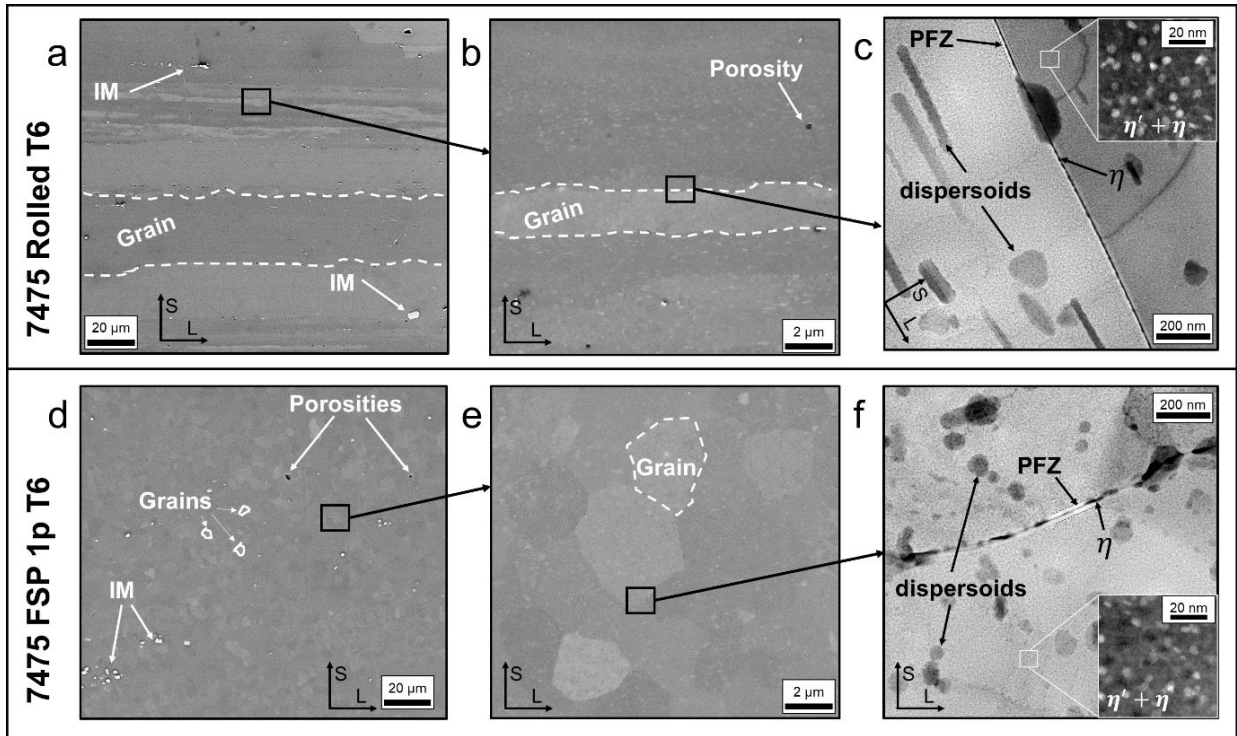


Figure 4: Microstructure of rolled BM-T6 (a,b,c) and FSP-T6 materials (d,e,f). SEM is used for overview of the microstructure (a,d), higher magnification on grains (b,e). BF-TEM is used in (c,f) to distinguish the PFZs and grain boundary η particles. Higher magnification zooms of HAADF-STEM in (c,f) allow the observation of the hardening precipitates in (c,f), precipitates being η' and η according to Liu et al. [6], Su et al. and Wang et al. [7]. L indicates for rolling direction, S short direction.

Figure 4a,b,c, shows the typical microstructure of high strength 7XXX Al alloys. BM-T6 alloy presents elongated grains of $25 \pm 20 \mu\text{m}$ thickness (in short direction), up to $300 \mu\text{m}$ wide (in transverse direction) and up to $700 \mu\text{m}$ long (in rolling direction). Coarse iron-rich IM and porosities are identified in **Figure 4**. The bright field TEM image of **Figure 4c** shows aligned coarse MgZn_2 η precipitates inside the precipitate free zones (PFZs) at grain boundaries. Coarser particles of roughly 50 nm are Cr-rich dispersoids (see supplementary **Figure S4**). Fine η' and η precipitates are homogeneously distributed (insert at **Figure 4c**) within the aluminium matrix, as expected for these alloys [6].

Figure 4d,e,f shows the microstructure of the FSPed-T6 alloy. Grains have an equivalent diameter of $2.5 \pm 0.5 \mu\text{m}$. In **Figure 4f**, the fine precipitates obtained after FSP-T6 heat treatment are similar to BM-T6 (see the TEM dark field zoom inset of **Figure 4f**). **Figure 4f** displays a grain boundary, where preferential precipitation occurs, leading to the formation of coarse η precipitates and PFZ.

The mean equivalent diameter of the matrix hardening precipitates is $2.3 \pm 1.6 \text{ nm}$ for the BM-T6 alloy and $3.2 \pm 1.0 \text{ nm}$ for the FSPed-T6 material. Finally, the PFZ width is measured as 24 nm for both the BM-T6 alloy and FSPed-T6 material.

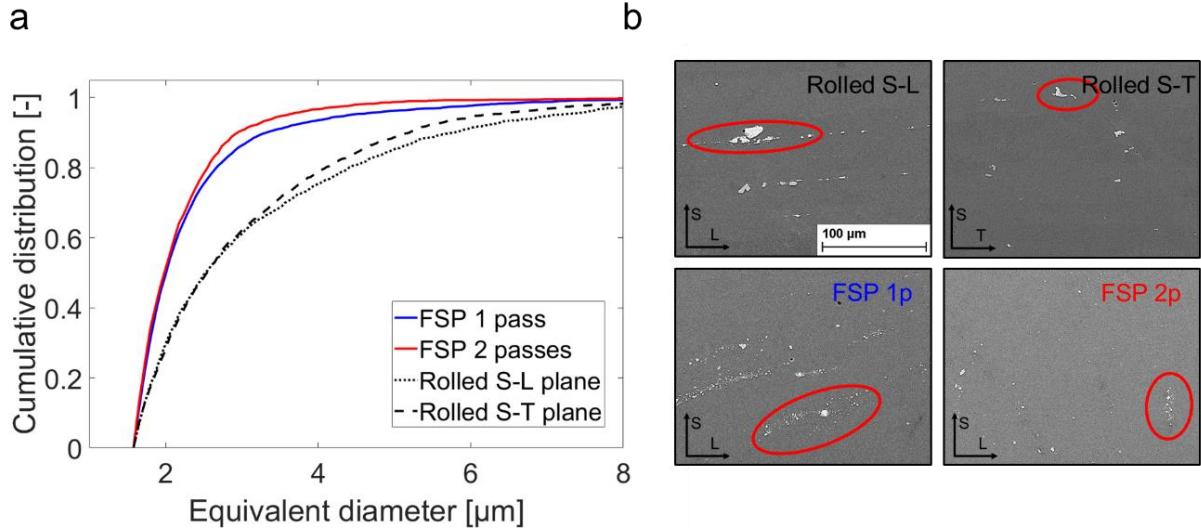


Figure 5: a) Cumulative distributions of intermetallic particles in the matrix (min detected size = 1.55 μm). b) Qualitative effect of cluster (highlighted with red ellipse) dispersed by FSP (1 and 2 pass) in NZ centre. Some clusters of particles are formed after 1 pass because of initial IM breakage, then the cluster size is reduced after the second pass. L states for rolling direction, S for short direction and T for transverse direction.

Figure 5a presents the cumulative size distributions (area-weighted) for the intermetallic particles based on SEM images. 15% of the IMs in the BM are larger than 5 μm in the short-rolling S-L plane. After FSP, only 4% and 1% of IMs are larger than 5 μm for 1 and 2 pass FSP, respectively. This indicates that the large IM particles are broken into smaller fragments during FSP. **Figure 5b** qualitatively displays the initial clusters of IM and the homogeneous re-distribution of broken fragments with increasing FSP passes. Clusters remain visible after one FSP pass due to the breakage of initial IMs, while the second pass significantly homogenizes the IM distribution. This is in good agreement with previous work performed on 6XXX Al Alloys [14].

Figure 6a,b,c shows that the fracture surface of BM-T6 (loading along T-dir) is affected by the initial elongated grains. Grain decohesion is visible (green arrows in **Figure 6b,c**). Some coarse precipitates are left on the detached surfaces (**Figure 6c**). Brittle impurities are found in coarse dimples (red arrows in **Figure 6b,c**). Finally, very fine dimples are identified by a blue arrow on **Figure 6c**. These observations are in accordance with the final transgranular microcracks coalescence presented in literature [5][10] and detailed above.

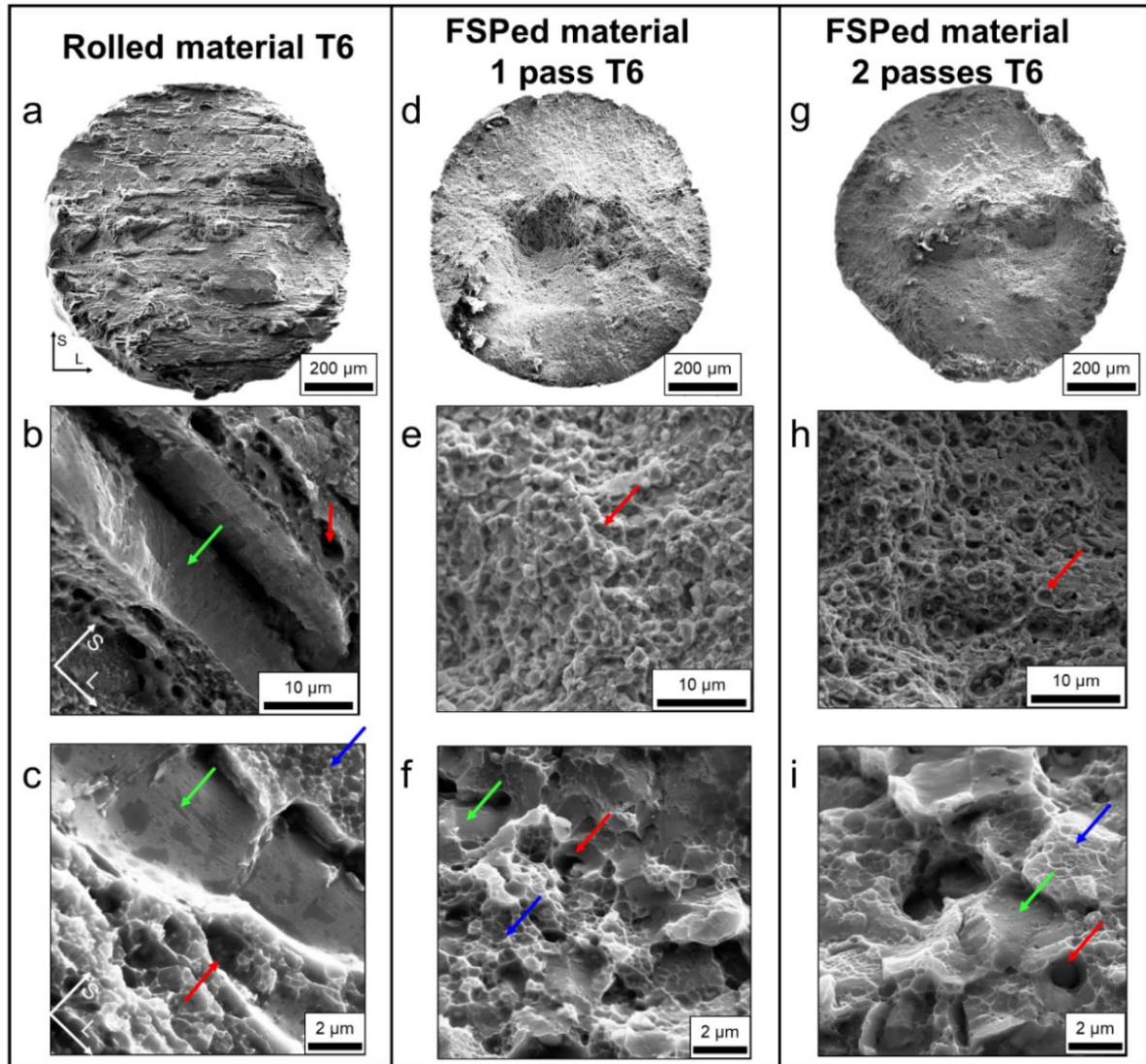


Figure 6: Fractography observed with SEM of BM-T6 (a,b,c), 1 pass FSP-T6 (d,e,f) and 2 pass FSP-T6 (g,h,i). The entire broken surfaces are visible on (a,d,g). Higher magnification views allow distinguishing coarse dimples (red arrows), finer dimples (blue arrows) and dimple-free regions related to grain boundary decohesion (green arrow).

Figure 6d,e,f displays the fracture surface of 1 pass FSP-T6 material. Coarse grains decohesion is not observed, in contrast to BM. Instead, a higher dimple density (red arrow in **Figure 6e**) and a mix of dimple-free and fine dimple zones (green and blue arrows in **Figure 6f**, respectively) are observed. The higher fraction of the total area covered by dimples (indicative of a void nucleation, growth and coalescence process) is in good agreement with the significant ductility improvement (**Figure 3a**). Oppositely, the BM shows extended dimple free areas, indicative of grain decohesion.

Figure 6g,h,i shows the 2 pass FSP-T6 material. Fine dimples are also formed as for the 1 pass sample (red arrows in **Figure 6h,i**). Again, the fracture surface presents alternatively smooth (green arrow) and fine dimples areas (blue arrow) as seen in **Figure 6i**, similarly to the 1 pass material.

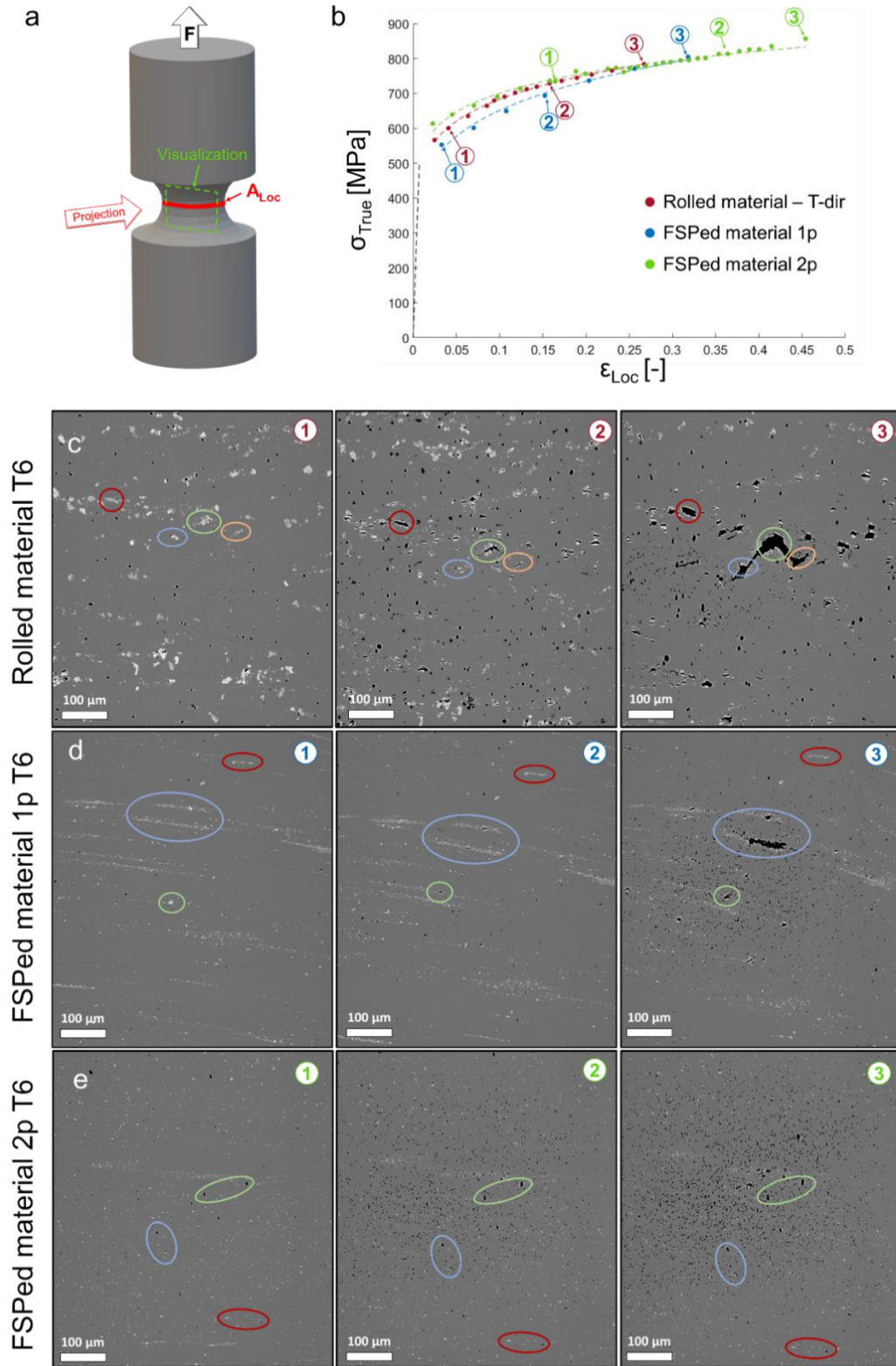


Figure 7: a) Schematic of in-situ tensile test during X-ray microtomography and visualization zone. b) Tensile curves of the in-situ tensile samples and identification of presented scans: c-e in relation to the reduced section ϵ_{Loc} of the tensile test sample. Damage propagation in rolled material (c, 1-3), 1 pass FSP (d, 1-3) and 2 pass FSP (e, 1-3) materials. All conditions are in T6 state. The stress-strain values of 1-2-3 visualizations for each sample are identified on (b). Strains defined as $\epsilon_{Loc} = \ln(A_0/A_{Loc})$ with A_0 and A_{Loc} the initial and current sample reduced sections respectively. Influence of IM particles, porosities and clusters is highlighted with coloured ellipses.

Figure 7a illustrates the in-situ tensile test procedure and visualization zone. The evolution of the minimum cross-sectional area (A_{Loc}) provides an estimate of local true tensile strain ($\epsilon_{Loc} = \ln(A_0/A_{Loc})$) and of true macroscopic axial stress ($\sigma_{True} = F/A_{Loc}$). **Figure 7b** displays the true stress versus local strain curves for the three investigated samples in T6 condition. **Figure 7c,d,e** shows visualizations of the voids (black) and IM particles (white) within the matrix (gray) in the middle of the tensile test specimens. The visualizations are created by taking the maximum intensity projection (MIP) of an X-ray microtomographic image of the sample over an 8 μm thick slab. The segmented voids have been overlaid on the projection.

Figure 7c shows the progressive damage of the BM-T6 loaded along the transverse direction. **Figure 7c-1** shows the initial microstructure, presenting several clusters of IM particles and initial porosities remaining from casting. The coarse IM particles contained in marked clusters break first, as shown in **Figure 7c-2**, leading to early crack coalescence inside some clusters. Before final failure, **Figure 7c-3** shows the crack propagation between clusters, with a 45° crack inclination.

Figure 7d shows the damage evolution after 1 pass FSP-T6. **Figure 7d-1** confirms that stirring reduces IM size, but clustering of IM fragments is still observed. Initial porosities are also reduced compared to BM. Voids nucleate on remaining coarse IM (**Figure 7d-2**) and early propagation within residual clusters is observed (**Figure 7d-3**).

Figure 7e shows that the IM fragments are more homogeneously distributed after 2 pass FSP, and clusters are not observed anymore. Numerous voids nucleate homogeneously throughout the microstructure (**Figure 7e-2**), and final strain at fracture is higher due to lower influence of IM clusters.

4. Discussion

The low ductility (i.e. low fracture strain) of T6 rolled material remains a limitation for forming as well as for crashworthiness. **Figure 3** reveals the impressive ductilization of FSPed Al 7475 at full strength compared to BM-T6 alloy, also confirmed for Al 7075 alloy (supplementary **Figure S3**).

In addition to the grain refinement by FSP (**Figure 4**), the IM size is also decreased due to breakage by stirring (**Figure 5a**). The IM fragments are then progressively dispersed (**Figure 5b**), in good agreement with observations on FSPed Al 6056 [14]. The IM size reduction and homogenization of particles distribution are also observed in the X-ray tomography scans of the rolled and FSPed materials (see **Figure 7c,d,e**).

Consequently, FSPed materials are significantly less prone to damage nucleation because of smaller IMs (**Figure 7d,e**), as explained by the classical size effect associated with the fracture of brittle particles. [10]. A second FSP pass enhances the homogeneity of the IM spatial distribution, reducing clusters. Heterogeneous void distribution favours microcracks propagation due to enhanced interaction of stress fields between closely spaced voids [24]. Crack propagation is therefore postponed for the more homogenous distribution of voids in the FSPed materials (see **Figure 7**),

because their interaction is weaker. Higher fracture strain levels are reached compared to the BM (**Figure 3** and **Figure 7b**).

Beside the IM redistribution and size reduction, FSP-T6 also affects crack propagation mechanisms. Looking at BM-T6, intergranular crack propagation between the rolled grains is identified in **Figure 6b,c** (green arrows). This behavior confirms the detrimental effect of PFZs located at grain boundaries on the fracture properties of 7XXX series alloys [5]. **Figure 6a** shows that crack propagation occurs by decohesion over large scales until the final failure of the material, as the entire broken surface is marked by GB decohesion. Coarse precipitates (greater than 100 nm) are left on the fracture surfaces (**Figure 6c**). In addition to the intergranular crack propagation, remaining grains or ligaments fail by shearing mechanism. Damage coalescence and crack propagation finally result in a flat and 45° tilted fracture plane, as observed in **Figure 7c-3** right before failure, in accordance with Ludtka *et al.* [5].

According to **Figure 3**, the rolled material has anisotropic properties. Grain orientation, IM particles and clusters are affecting the tensile performances, as described in [25]. BM-T6 has lower yield strength but higher fracture strain in the rolling direction. The IM clusters alignment in the rolling direction (**Figure 5b**) clearly affects tensile crack propagation, see **Figure 7c**.

As observed in **Figure 4**, FSP leads to a significant grain refinement and an equiaxed grain morphology, suppressing anisotropy. A change in crack propagation scenario is thus expected due to the suppression of straight and elongated grain boundaries. Indeed, FSP-T6 materials (**Figure 6d,g**) show significant changes in fracture surface morphology compared to the BM-T6 (**Figure 6a**). No more extended intergranular crack propagation is detected. However, the FSP-T6 material also presents PFZs similar with the PFZs observed within the BM. FSP-T6 also contains coarse precipitates at grain boundaries similarly to the T6 rolled microstructure, see **Figure 4c,f**. It is thus expected to also observe grain decohesion, but evidences of decohesion are not found. The competition between transgranular and intergranular crack propagation was investigated on 7XXX alloys [26]. Scheyvaerts *et al.* showed that increasing the ratio of yield strength of grain interior to PFZ favoured intergranular fracture [26]. However, this ratio does not vary after FSP-T6. Pardoen *et al.* simulated the influence of PFZ geometrical parameters on fracture, showing that PFZ width and precipitates spacing and size may influence failure [27]. Now, these parameters are not significantly different between FSP-T6 and BM-T6 conditions of the present work. More interestingly, increasing the relative PFZ thickness compared to grain size is responsible of higher ductility despite a limited effect on crack propagation mechanism [27]. This explains well our results: FSP-T6 PFZ are similar to BM-T6 PFZ (**Figure 4c,f**) but grain size is significantly reduced (**Figure 4b,d**), increasing the PFZ versus grain size ratio. Consequently, both 1 and 2 pass FSP-T6 materials show larger amounts of voids under the fracture surface (**Figure 7c,d,e**), leading to transgranular void coalescence, in contrast to the rolled material that is characterized by substantial intergranular cracks.

5. Conclusion

In summary, the obtained FSP-T6 materials succeed to enhance the total fracture strain by 180%, with an unchanged yield strength of about 500 MPa (T6 state). FSP allows the reduction of impurities size and a better distribution of the IM clusters, this distribution being homogenized after the second FSP pass. The applied T6 heat treatment restores the hardening precipitation without affecting the refined grains (i.e. without abnormal grain growth). Despite the existence of PFZs and grain boundary precipitates in both rolled and FSPed-T6 materials, a significant change in damage nucleation and crack propagation is observed. The FSP-T6 microstructure first postpones the damage nucleation because of smaller and more resistant brittle IM fragments. Then, the microcracks formation within IM clusters is delayed or even suppressed with the second pass. Finally, the formation of elongated cracks following the grain boundaries in the rolled material is fully inhibited after FSP due to grain refinement. This work has proved that FSP can be locally applied to avoid premature cracking during 7XXX aluminium alloys forming.

Acknowledgments

This research work has been supported by the European Research Council (ERC) under the European Union's Horizon 2020 research and innovation program (grant agreement n716678). M.B.L., F.H. and H.I. are mandated by the Belgian National Fund for Scientific Research (FSR-FNRS). This work was supported by the FNRS under Grant CDR-J011320F.

We acknowledge the Paul Scherrer Institut, Villigen, Switzerland for provision of synchrotron radiation beamtime at the TOMCAT beamline X02DA of the SLS.

Data availability

The raw/processed data required to reproduce these findings cannot be shared at this time as the data also forms part of an ongoing study.

References

- [1] P. Dungore, A. Agnihotri, Special heat treatment practices for aerospace aluminum alloys, *Heat treating progress* May/June 2008, 35-38.
- [2] Tomoya Aoba, Masakazu Kobayashi, Hiromi Miura, Effects of aging on mechanical properties and microstructure of multidirectionally forged 7075 aluminum alloy, *Materials Science and Engineering A* 700, (2017) 220-225.
- [3] J.-Q. Su, T.W. Nelson, R. Mishra, M. Mahoney, Microstructural investigation of friction stir welded 7050-T651 aluminium, *Acta Materialia* 51, (2003) 713-729.
- [4] Paul A. Rometsch, Yong Zhang, Steven Knight, Heat treatment of 7xxx series aluminium alloys - Some recent developments, *Trans. Nonferrous Met. Soc. China* 24, (2014) 2003-2017.
- [5] Gerard M. Ludtka and David E. Laughlin, The Influence of Microstructure and Strength on the Fracture Mode and Toughness of 7XXX Series Aluminum Alloys, *Metallurgical Transactions A*, Volume 13A, (March 1982) 411-425.
- [6] Shengdan Liu, Qun Li, Huaqiang Lin, Lin Sun, Tao Long, Lingying Ye, Yunlai Deng, Effect of quench-induced precipitation on microstructure and mechanical properties of 7085 aluminum alloy, *Materials and Design* 132 (2017) 119-128.
- [7] Yichang Wang, Xiaodong Wu, Lingfei Cao, Xin Tong, Yan Zou, Qianqian Zhu, Songbai Tang, Hui Song, Mingxing Guo, Effect of Ag on aging precipitation behavior and mechanical properties of aluminum alloy 7075, *Materials Science & Engineering A* 804 (2021) 140515.
- [8] Eric Maire, Suxia Zhou, Jerome Adrien, Marco Dimichiel, Damage quantification in aluminium alloys using in situ tensile tests in X-ray tomography, *Engineering Fracture Mechanics* 78 (2011) 2679–2690.
- [9] F. Hannard, T. Pardoen, E. Maire, C. Le Boulbot, R. Mokso, A. Simar, Characterization and micromechanical modelling of microstructural heterogeneity effects on ductile fracture of 6xxx aluminium alloys, *Acta Materialia* 103 (2016) 558-572.
- [10] N. Kamp, I. Sinclair, and M.J. Starink, Toughness-Strength Relations in the Overaged 7449 Al-Based Alloy, *Metallurgical and Materials Transactions A* Volume 33A, April 2002, 1125-1136.
- [11] Yichang Wang, Xiaodong Wu, Lingfei Cao, Xin Tong, Malcolm J. Couper, Qing Liu, Effect of trace Er on the microstructure and properties of Al–Zn–Mg–Cu–Zr alloys during heat treatments, *Materials Science & Engineering A* 792 (2020) 139807.
- [12] R.S. Mishra, Z.Y. Ma, Friction stir welding and processing, *Materials Science and Engineering R* 50, (2005) 1-78.
- [13] A. Heidarzadeh, S. Mironov, R. Kaibyshev, G. Çam, A. Simar, A. Gerlich, F. Khodabakhshi, A. Mostafaei, D.P. Field, J.D. Robson, A. Deschamps, P.J. Withers, Friction stir welding/processing of metals and alloys: A comprehensive review on microstructural evolution, *Progress in Materials Science*.

- [14] F. Hannard , S. Castin, E. Maire, R. Mokso, T. Pardoen, A. Simar, Ductilization of aluminium alloy 6056 by friction stir processing, *Acta Materialia* 130, 2017, 121-136.
- [15] N. Kamp, A. Sullivan, R. Tomasi, J.D. Robson, Modelling of heterogeneous precipitate distribution evolution during friction stir welding process, *Acta Materialia* 54, (2006) 2003-2014.
- [16] C. Fuller, M. Mahoney, M. Calabrese, L. Micono, *MSE. A* 527 (2010) 2233-2240.
- [17] Pratip Roy, Subhash Singh & Kaushik Pal, Enhancement of mechanical and tribological properties of SiC- and CB reinforced aluminium 7075 hybrid composites through friction stir processing, *Advanced Composite Materials*, 2017.
- [18] Friction stir welding and processing R.S. Mishra, Z.Y. Ma, *Materials Science and Engineering R* 50 (2005) 1-78.
- [19] Matthieu B. Lezaack, Aude Simar, Avoiding abnormal grain growth in thick 7XXX aluminium alloy friction stir welds during T6 post heat treatments, *Materials Science & Engineering A* 807 (2021) 140901.
- [20] Kai Li, Hosni Idrissi, Gang Sha, Min Song, Jiangbo Lu, Hui Shi, Wanlin Wang, Simon P. Ringer, Yong Du, Dominique Schryvers, Quantitative measurement for the microstructural parameters of nano-precipitates in Al-Mg-Si-Cu alloys, *Materials Characterization* 118 (2016) 352-362.
- [21] E Maire, C Le Burlot, J Adrien, A Mortensen, R Mokso, 20 Hz X-ray tomography during an in situ tensile test, *International Journal of Fracture* 200 (1), 3-12.
- [22] Luc Salvo, Michel Suéry, Ariane Marmottant, Nathalie Limodin, Dominique Bernard, 3D imaging in material science: Application of X-ray tomography, *C. R. Physique* 11 (2010) 641–649.
- [23] A. Simar, Y. Bréchet, B. de Meester, A. Denquin, T. Pardoen, Microstructure, local and global mechanical properties of friction stir welds in aluminium alloy 6005A-T6, *Materials Science and Engineering A* 486 (2008) 85-95.
- [24] F. Hannard, A. Simar, E. Maire, T. Pardoen, Quantitative assessment of the impact of second phase particle arrangement on damage and fracture anisotropy, *Acta Materialia* Volume 148 (2018) 456-466.
- [25] J.B. Jordon, M.F. Horstemeyer, K. Solanki, J.D. Bernard, J.T. Berry, T.N. Williams, Damage characterization and modeling of a 7075-T651 aluminum plate, *Materials Science and Engineering A* 527 (2009) 169-178.
- [26] F. Scheyvaerts, P.R. Onck, Y. Bréchet, T. Pardoen: Multiscale simulation of the competition between intergranular and transgranular fracture in 7000 alloys, 11th International Conference on Fracture 2005, *ICF11* Volume 6, (2005) 4164-4169.
- [27] T. Pardoen, D. Dumont, A. Deschamps, Y. Brechet, Grain boundary versus transgranular ductile failure, *Journal of the Mechanics and Physics of Solids* 51, (2003) 637 –665.